Monthly Notices
of the
ROYAL ASTRONOMICAL SOCIETY

MNRAS **441,** 431–441 (2014) doi:10.1093/mnras/stu497

Interaction of a galactic wind with halo gas and the origin of multiphase extraplanar material

Mahavir Sharma,[1]★ Biman B. Nath,[1] Indranil Chattopadhyay[2] and Yuri Shchekinov[3]

[1]*Raman Research Institute, Sadashivanagar, Bangalore 560080, India*
[2]*Aryabhatta Research Institute of Observational Sciences, Manora Peak, Nainital 263002, India*
[3]*Department of Physics, Southern Federal University, Rostov on Don 344090, Russia*

Accepted 2014 March 8. Received 2014 February 25; in original form 2013 June 19

ABSTRACT

We study the interaction of a galactic wind with hot halo gas using hydrodynamical simulations. We find that the outcome of this interaction depends crucially on the wind injection density and velocity. Various phases of extraplanar media such as infalling clouds, outflowing clouds and O VI regions can originate in the interaction zones of wind with the halo gas, depending on the injection velocity and density. In our simulations, the size of the clouds is of the order of 100 pc. The total mass contained in the clouds is 10^5–10^7 $M_\odot$ and they have a normal distribution of velocities in the galactic standard of rest frame. For high injection density and velocity, a significant number of clouds move outwards and resemble the case of cold neutral outflows. Furthermore, a 10^5–10^6 K phase is formed in our simulations, which has a column density $\sim 10^{18}$ cm^{-2} and resembles the observed O VI regions. The injection velocity and density are linked with the mass-loading factor of the outflow, efficiency of energy injection due to supernovae and star-formation rate. Comparison of the predicted morphology of extraplanar gas with observations can serve as a useful diagnostic for constraining the feedback efficiency of outflows.

Key words: galaxies: evolution – galaxies: haloes – galaxies: starburst – X-rays: galaxies.

1 INTRODUCTION

Disc galaxies contain a substantial amount of baryonic matter outside the disc and this extraplanar material has become an important problem to study for a number of reasons. Theoretically, since the pioneering articles by Spitzer (1956) and Pickelner & Shklovsky (1958) that invoked the presence of high-pressure 'coronal' gas outside the disc, its existence has been debated. Early works on galaxy formation suggested that the collapse of haloes should lead to shock-heated gas in the halo. However, various physical processes during the galactic evolution, such as star formation, galaxy mergers and stripping by the intergalactic medium (IGM), would have played a significant role in shaping the extraplanar material that is observed today. Recent observations have detected this extraplanar gas in H I (Swaters, Sancisi & van der Hulst 1997), Hα (Rossa et al. 2004; Voigtländer et al. 2013) and X-rays (Wang 2001; Strickland et al. 2004). The extraplanar gas and its different phases appear in the literature under different names, a few of which are listed below.

Hot halo gas. In the standard cold dark matter scenario of structure formation in the Universe, baryonic gas falls into dark matter potentials and gets heated to the virial temperature (Silk 1977; White & Rees 1978; White & Frenk 1991). The gas then cools radiatively and if the temperature is such that the cooling is rapid (for $T \leq 10^6$ K), for the case of low-mass galaxies, then no accretion shock develops outside the evolving disc and most of the halo gas remains at a temperature lower than the virial temperature (Binney 1977; Birnboim & Dekel 2003). This scenario of 'cold accretion' for low-mass galaxies has received some observational support in recent years. In massive galaxies, the hot halo gas is believed to cool slowly and eventually to form warm (10^4 K) clouds embedded in a large-scale hot corona. These clouds could fall on to the disc in the form of high-velocity clouds (e.g. Maller & Bullock 2004; Kauffmann et al. 2006). Numerical simulations have also shown that disc galaxies are embedded in hot gaseous haloes and that the X-ray luminosity of the halo gas should scale with galactic mass. However, this hypothetical hot halo gas is yet to be observed (Rasmussen et al. 2009, and references therein) and observations of extraplanar gas have so far been limited to regions close to the disc and bulge or around active star-forming regions (e.g. Wang 2007). Moreover, if the halo does contain a large amount of gas, it could potentially explain the missing baryon problem, which states that more than 80 per cent of baryons are unaccounted for by collapsed gas and stars in galaxies (Fukugita, Hogan & Peebles 1998; Anderson & Bregman 2010).

★ E-mail: mahavir@rri.res.in

Galactic wind. The subsequent evolution of halo gas is thought to be governed by both the inflow of gas from the IGM and energy injection processes in the disc. Many star-forming galaxies have been observed to contain a large amount of outflowing gas (see Veilleux, Cecil & Bland-Hawthorn 2005, for a review). Early observations of outflowing gas in M82 led to the development of Parker-type steady winds with energy and mass injection from supernovae (SNe; Burke 1968; Johnson & Axford 1971; Chevalier & Clegg 1985). These calculations showed that fast, steady winds with speeds exceeding 10^3 km s^{-1} can be generated from the central regions of M82-type starburst galaxies. Wang (1995) explored steady wind solutions with radiative cooling and showed that O VI emission in haloes can arise from thermally unstable outflows. Tomisaka & Bregman (1993) studied SN-driven outflows and their interaction with halo gas and estimated the extended X-ray emission from an M82-type galaxy. Detailed numerical simulations have been carried out focused on the properties of outflows and their implication for IGM enrichment (Suchkov et al. 1994, 1996; Mac Low & Ferrara 1999; Dalla Vecchia & Schaye 2008; Hopkins, Quataert & Murray 2012). Recently, Sharma & Nath (2013) studied steady galactic winds from dark matter haloes with Navarro–Frenk–White (NFW) density profiles (Navarro, Frenk & White 1997) and found that SNe can drive outflows from dwarf galaxies and that active galactic nuclei (AGN) power outflows with speeds exceeding 10^3 km s^{-1} in massive galaxies, e.g. ultraluminous infrared galaxies (ULIRGs). They also found that winds from intermediate-sized galaxies that are in a quiescent mode of star formation (e.g. the Milky Way) cannot escape the halo. As a consequence of this, one can explain the observed trend of the stellar to halo mass ratio.

Outflowing cold/warm clouds. The outflowing gas is often observed to contain a clumpy component that contains neutral or partially ionized atoms at 10^4 K (e.g. Martin 2005). In starbursts such as M82, molecular clouds and filaments have also been observed in the outflowing gas (Veilleux, Rupke & Swaters 2009). The dynamics of these clouds offers useful clues to the formation and evolution of the outflowing gas and recently has been used to discuss various physical processes that drive these clouds. Martin (2005) and Murray, Quataert & Thompson (2005) suggested that radiation pressure on dust grains embedded in these clouds may play an important role in their dynamics (see also Sharma, Nath & Shchekinov 2011; Chattopadhyay et al. 2012). Sharma & Nath (2012) showed that radiation pressure becomes important only for galaxies with mass $\geq 10^{12}$ M$_\odot$ and with high SFR, e.g. ULIRGs. However, the formation process of these clouds remains uncertain. Marcolini et al. (2005) argued that the clouds are likely to be shredded by Kelvin–Helmholtz instability and/or evaporation due to thermal conduction, with a time-scale ≤ 1 Myr. It is therefore a puzzle that these clouds are often observed at distances of several kpc, since the travel time (assuming the speed to be a few hundred km s^{-1}) is likely to be $\sim$10 Myr. Nath & Silk (2009) and Murray, Ménard & Thompson (2011) have suggested a scenario in which radiation pressure pushes a shell of gas and dust, which then fragments after being accelerated by thermal pressure from SNe ejecta.

High-velocity clouds. The extraplanar gas is also affected by disc interstellar medium (ISM) processes in another way. In the galactic fountain model (Shapiro & Field 1976; Bregman 1980), partially ionized gas is launched from the disc by the effect of multiple SNe and, after travelling some distance in the halo, it falls back to the disc.

An important problem in this regard is that of the formation of clouds in the extraplanar gas, which are observed as either high-velocity clouds (HVC) or O VI clouds. Bregman (1980) argued that HVCs could form from the condensation of galactic fountain material (but see Ferrara & Einaudi 1992). However, this idea cannot explain the fact that the observed metallicity is less than that of the disc ISM (van Woerden & Wakker 2004). This is particularly important for HVCs that are more than $\sim$5 kpc away from the Milky Way disc, which have low metallicity ($Z \sim 0.01$–$0.2\,Z_\odot$). Binney, Nipoti & Fraternali (2009) have argued that thermal instability is not efficient in moving fountain gas and clouds are rather likely to form, due to the interaction of ejected disc material with pre-existing halo gas. Recently, using high-resolution simulations, Marinacci et al. (2010) have shown that cold clouds can condense out of a galactic fountain moving through halo gas (see also Marinacci et al. 2011). Wakker et al. (2005) found that O VI absorption associated with HVCs can arise from the interface between a HVC and coronal gas. However we note that, in HVCs nearer than $\sim$10 kpc, there can be a mixture of components from the Galactic ISM, the interface region with halo gas or gas from the Local Group. Thus, the overall picture is tangled because of contamination at lower heights connected with interaction of falling gas with the extended gas of the galactic corona or by the flows generated by internal galactic processes.

Circumgalactic medium. The gaseous content of a spiral galaxy outside the disc but within the halo of dark matter, formed and shaped by various processes of accretion and outflows as mentioned above, is generally referred to as the circumgalactic medium (CGM). This refers to the reservoir of gas at distances $\sim$100–250 kpc. However, its existence and its relation to processes near and in the disc are not yet fully understood. Although outflowing gas is observed near the disc, it is not clear how far this gas propagates nor the nature of the interaction with pre-existing gas in the halo. It is uncertain whether most of the wind material escapes the halo or is retained in the halo and then whether or not most of this gas eventually falls back to the disc. A large amount of hot gas in a halo can potentially distort cosmic microwave background radiation through the Sunyaev–Zel'dovich effect (e.g. Majumdar, Nath & Chiba 2001). The low density of the CGM makes it an elusive component to observe, but recently it has been detected through absorption in the line of sight of background quasars. Tumlinson et al. (2011) detected a large amount of O VI absorbing gas at $T \sim 10^{5.5}$ K in galaxies with moderate SFR. However, its spatial extent and the total gas (and metal) content still need to be measured with enough accuracy to constrain theoretical models.

In the present article, we address the question of the origin of high-velocity clouds, circumgalactic material and the cold clumps in galactic winds, as a result of the interaction of a steady galactic wind with the relic halo gas distribution using 2D simulations. Our aim is to show that all these constituents of extraplanar material may have a common origin, which is the interaction zone between the galactic outflow and hot gas in a halo.

The remainder of the article is organized as follows. In Section 2 we describe our simulation set-up, including the initial and boundary conditions. In Section 3 we give analytical estimates for the dynamics of the interaction zone and compare the time-scales relevant for the problem. In Section 4 we present the results of our model runs and then in Section 5 we discuss our results, along with the implications.

2 SIMULATION SET-UP

In this work we use the cylindrical (R, ϕ, z) coordinate system with cylindrical symmetry around the z-axis, in which the distance (r) to any random point can be calculated from the in-plane radius (R) and height (z) by using $r = \sqrt{R^2 + z^2}$. The unit of density in

our simulation is 1.67×10^{-24} g cm^{-3}. The unit of velocity is 100 km s^{-1} and the unit of distance is kpc. Hence, the unit of time in the present simulation is 9.5 Myr.

2.1 Initial and boundary conditions

We populate the halo with an isothermal gas distribution in hydrostatic equilibrium in a NFW dark matter halo. The gravitational potential for a NFW dark matter halo is given by

$$\Phi(r) = -2v_s^2 \frac{\ln(1 + r/r_s)}{r/r_s}, \quad (1)$$

where $v_s^2 = GM_{200}/[2r_s f(c)]$, with $f(c) = \ln(1 + c) - c/(1 + c)$ and $r_s = r_{200}/c$. Here $c(= 10)$ is the halo concentration parameter, r_{200} is the virial radius and M_{200} is the virial mass. We consider a halo of mass 10^{12} M$_\odot$ in our simulation. The corresponding circular speed is ≈180 km s^{-1} according to the definition given in Navarro et al. (1997) and the escape speed at the centre is $2v_s$, i.e. a value of 530 km s^{-1}.For the gravitational potential in equation (1), the hydrostatic density profile is given by

$$n(r) = n_0 \exp\left[-\frac{\mu m_p(\Phi(r) - \Phi(r_b))}{kT}\right], \quad (2)$$

where n_0 is the density at the base, which is also the maximum value of initial density, and $\mu(= 0.6)$ is the mean molecular weight. We take the density at the base $n_0 = 10^{-3}$ cm^{-3}. We note that the similar cored density profiles, with a central density $\sim 10^{-3}$ cm^{-3}, have been deduced for the gas in the halo of the Galaxy in recent studies (Fang, Bullock & Boylan-Kolchin 2013; Putman, Peek & Joung 2012; Maller & Bullock 2004). The above profile is characterized by the temperature T. We consider a temperature, $T \approx 3 \times 10^6$ K, that is approximately the virial temperature for a Milky Way size halo with mass 10^{12} M$_\odot$ considered in this simulation. Observations also indicate a similar temperature for the hot gas in the halo of the Galaxy (Hagihara et al. 2010; Fang et al. 2013). In Fig. 1, we have shown the density profile of halo gas for the halo of mass 10^{12} M$_\odot$ considered in this work.

We set up a simulation box in which R ranges from 0 to R_{max} and z goes from r_b to z_{max}, where r_b is the launching height. Therefore the simulation box covers the right half of the upper hemisphere of the galactic halo. The spiral disc lies at the base of the hemisphere and outside ($z < r_b$) our computation box. We use the density profile given by equation (2) for the outer boundaries at z^+_{max} and R^+_{max}, so that the initial hydrostatic distribution of gas does not change with time. At the lower z boundary, we once again use the density profile given in equation (2), except for a region satisfying $0 < R < r_b$, $z < r_b$, in which we inject the material with a specific density and velocity, as discussed below.

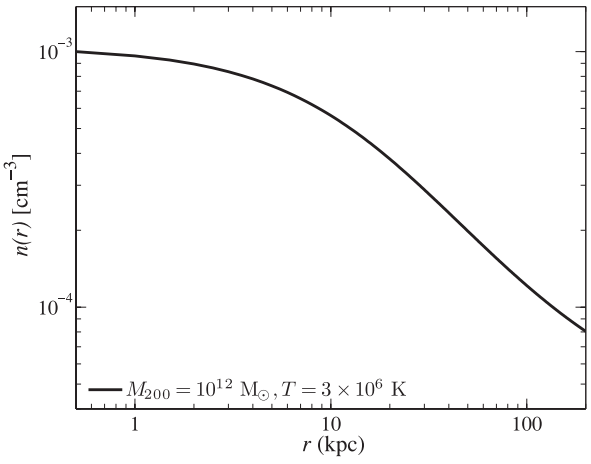

Figure 1. The density profile for the gas in the halo.

2.2 Injection parameters

The injection of wind gas is implemented by assuming that a supersonic wind enters the computation zone from below. We inject (continuously in time) gas with speed v_{inj} and density n_{inj} in a section of the lower boundary satisfying $0 < R < r_b$. The injected gas has a temperature corresponding to the sound speed (c_s), somewhat lower than the injection speed (v_{inj}), to ensure that the flow is in the supersonic regime. This value of v_{inj} will give a wind speed $v_{wind} \sim 2v_{inj}$, which can be understood simply by the fact that in the supersonic regime, as the wind diverges, the sound speed decreases to small values and the wind speed becomes the sum of the initial injection speed and the sound speed at the base. A supersonic injection right from the base implies that we have assumed a thermalization zone with dimensions $0 < R < r_b$, $0 < |z| < r_b$ centred on the galaxy in which energy and mass injection due to stellar processes occur. The size of the thermalization zone (r_b) is in principle a free parameter. Melioli & de Gouveia Dal Pino (2004) consider r_b in the range 100–700 pc. In the present study we work with a fixed value of $r_b = 500$ pc. We use a range of injection speeds and densities. The injection speed and density are functions of the energy injection rate ($\dot{E}$), mass-loading rate ($\dot{M}$) and SFR. If we consider the thermalized injection zone to be approximately spherical with radius r_b, then the mass-loading rate for the wind can be approximated as $\dot{M} = 4\pi m_p n_{inj} v_{inj} r_b^2$. Furthermore, one compares this mass-loss rate with the SFR by defining a load factor η, which can be written as

$$\eta = \left(\frac{\dot{M}}{\mathrm{M}_\odot\ \mathrm{yr}^{-1}}\right) \mathrm{SFR}^{-1}, \quad (3)$$

where SFR is in units of M$_\odot$ yr^{-1}. Energy injection due to SNe depends on the rate of occurrence of SNe and therefore on the SFR. One can define the energy injection as ($\dot{E} = \epsilon f_{sn} E_{sn}$SFR) erg yr^{-1}. Here, ϵ is the efficiency of the energy injection, with a value that is 0.1 in normal situations, when most of the energy of SNe is lost via radiation, and can be as high as 0.5 for starburst galaxies like M82. f_{sn} is the fraction of SNe per unit solar mass of star formation and has a value of 1.26×10^{-2} for a Kroupa–Chabrier initial mass function (Chabrier 2003). $E_{sn} = 10^{51}$ erg is the energy yield of a single supernova. Using these values, we obtain the energy injection rate $\dot{E} = \epsilon(4 \times 10^{41})$ SFR erg s^{-1}. For the SN-driven wind, the energy injection rate is the mechanical luminosity of the wind and is related to the mass-loss rate by $\dot{E} = \frac{1}{2}\dot{M} v_{wind}^2 = 2\dot{M} v_{inj}^2$, where we have used $v_{wind} = 2v_{inj}$. Equating the above two definitions of $\dot{E}$, we obtain the following relation for the efficiency of energy injection (ϵ):

$$\epsilon = 0.8 \left(\frac{\dot{M}}{\mathrm{M}_\odot\ \mathrm{yr}^{-1}}\right)\left(\frac{v_{inj}}{500\ \mathrm{km\ s}^{-1}}\right)^2 \mathrm{SFR}^{-1}. \quad (4)$$

In the fourth column of Table 1, we have provided the quantity $\eta \times$ SFR, which is essentially the mass-loss rate, and in the fifth column we have provided $\epsilon \times$ SFR corresponding to each run. One can infer the value of η or ϵ for a particular case by dividing the values mentioned in the fourth and fifth columns by the SFR. For example, if SFR = 3 M$_\odot$ yr^{-1} in the case of *MG1*, we would have $\eta \approx 0.7$ and $\epsilon \approx 0.2$.

Table 1. The parameters of our runs. Combinations of $n_{\rm inj}$ and $v_{\rm inj}$ adopted for our runs are given in the second and third columns. In the fourth column we have provided the quantity $\eta \times$ SFR, which is essentially the mass-loss rate, and in the fifth column we have provided $\epsilon \times$ SFR corresponding to each run. One can infer the value of η or ϵ for a particular run by dividing the values mentioned in the fourth and fifth columns by the SFR (i.e. for an SFR of 3 $M_\odot$ yr^{-1} in case *MG1* we would have $\eta \approx 0.7$ and $\epsilon \approx 0.2$). In the last column, we have provided the dimensions of the simulation box. All of our runs except *MG1* have an implementation of equilibrium radiative cooling.

Name	$n_{\rm inj}$ (cm^{-3})	$v_{\rm inj}$ (km s^{-1})	$\eta \times$ SFR	$\epsilon \times$ SFR	box size (kpc $\times$ kpc)
MG1	0.1	300	2.23	0.64	10 $\times$ 20
MG2	0.1	300	2.23	0.64	10 $\times$ 20
MG3	1.0	400	29.78	15.12	20 $\times$ 40
MG4	2.0	600	89.34	102.56	50 $\times$ 100
MG5	0.5	500	18.61	14.84	50 $\times$ 100
MG6	1.2	500	44.67	35.61	50 $\times$ 100
MG7	0.05	500	1.86	1.48	20 $\times$ 40
MG8	0.4	350	10.41	4.06	20 $\times$ 40
MG9	2.0	350	52.03	20.32	20 $\times$ 40
MG10	0.1	400	2.97	1.52	20 $\times$ 40
MG11	0.1	500	3.72	2.96	50 $\times$ 100
MG12	0.5	500	18.58	14.81	50 $\times$ 100
MG13	0.01	200	0.15	0.02	10 $\times$ 20
MG14	10.0	300	223	67	10 $\times$ 20
MG15	5.0	200	74.3	9.5	10 $\times$ 20

2.3 Details of our runs

We use the publicly available hydrodynamic code PLUTO (Mignone et al. 2007). For our runs, we use the solver based on the total variation-diminishing Lax–Friedrich (TVDLF) scheme supplied with the code. PLUTO has a well-tested implementation of radiative cooling (Teşileanu, Mignone & Massaglia 2008), which is performed by solving the energy equation with an energy-loss term, which for this study is a function of density and temperature as given by Sutherland & Dopita (1993) in the case of equilibrium cooling. We assume solar metallicity for the wind and the halo gas in our simulation. The halo likely has a lower metallicity, but in this work we do not explore the effect of a two-component gas with different metallicities.

We have run the simulation for various values of initial and injection parameters. The quantitative details of the parameters involved in our runs are provided in Table 1. Various sets of parameters are chosen to study the dependence of the formation of a multiphase medium on the hot halo gas and wind properties. We set resolutions of 250 $\times$ 500, 500 $\times$ 1000 and 1000 $\times$ 2000, corresponding to box dimensions of 10 $\times$ 20, 20 $\times$ 40 and 50 $\times$ 100 kpc^2 respectively. Therefore, the smallest cell size in our simulations is 40 pc for the box with heights 20 and 40 kpc and 50 pc for the box with height 100 kpc. We find that clouds formed in our simulation have sizes roughly in the range 100–500 pc and hence the resolution is adequate to capture the clouds. We have also checked with a finer resolution (cell size=20 pc) and the cloud sizes are unaffected.

3 ANALYTIC CONSIDERATIONS

In this section we provide analytical estimates relevant for the simulations in this work. This problem has similarities with the case of a wind-blown bubble, where the stellar wind is expanding in a uniform-density medium (Weaver et al. 1977). However, there are some subtle differences between a stellar wind-blown bubble and the present case of a galactic wind interacting with halo gas. While in a stellar wind-blown bubble the ambient medium is denser than the wind, here the opposite holds true, at least for the initial evolution, when the wind density is larger compared with the ambient density. Also, the temperature of the ambient medium in this case is $\sim 10^6$ K, which is two orders of magnitude larger than the ISM temperature ($\sim 10^4$ K), relevant for a stellar wind-blown bubble. Another difference is the stratification in the density of the ambient halo gas. Because of the stratification, the outermost shock does not slow down quickly and the late-time evolution should not be given by a self-similar solution as described in Weaver et al. (1977). One should instead work out the dynamics after taking the density profile into account, as in Kompaneets (1960). Due to this effect, the free expansion phase of the wind lasts longer and, if the wind has enough mechanical luminosity that it crosses the scaleheight of the halo gas profile, it may keep expanding freely with the normal wind speed and eventually escape the halo. We quantify these aspects below.

In the general case of a supernova blast or a wind interacting with an ambient medium, there are three distinct phases of evolution. Initially there is the free expansion phase. When the swept-up mass becomes comparable to the mass in the wind, then the wind is obstructed by an outside mass, the free expansion phase ends and the wind enters the next phase of evolution, in which the motion can be described by a self-similar solution. This phase ends when radiative losses become significant and the system enters into a momentum-driven phase.

Let us perform a simple estimate for the distance ($r_{\rm f}$) at which the transition from a free wind phase to a self-similar phase is expected. It can be computed by equating the swept-up mass with the injected mass. For this rough estimate, we assume the injection region to be spherical with radius $r_{\rm b}$, since $r_{\rm b}$ is much smaller than the length-scale of winds involved in our simulations. This gives

$$\int_{r_{\rm b}}^{r_{\rm f}} (4\pi r^2) m_{\rm p} n(r)\, {\rm d}r = \int_0^{t_{\rm f}} 4\pi m_{\rm p} n_{\rm inj} v_{\rm inj} r_{\rm b}^2\, {\rm d}t, \quad (5)$$

where $n(r)$ is the density profile of the gas in the halo as given by equation (2) and $t_{\rm f}$ is the time that marks the end of the free expansion phase. The left-hand side in the above equation is the swept-up mass of the halo gas and the right-hand side is the total injected mass till the time $t_{\rm f}$. $r_{\rm f}$ is related to $t_{\rm f}$ via $r_{\rm f} = \int_0^{t_{\rm f}} v_{\rm wind}\, {\rm d}t$. As explained in Section 2.2, in the supersonic regime the wind speed is $v_{\rm wind} \sim 2v_{\rm inj}$, therefore $t_{\rm f} = r_{\rm f}/(2v_{\rm inj})$. We find that $r_{\rm f}$ is roughly constant for $n_{\rm inj} \leq 0.1$ cm^{-3} and lies in the range 2–5 kpc, but it increases to $\sim$30 kpc for $n_{\rm inj} \sim 1$ cm^{-3}. This implies that, for low injection density, the free expansion phase ends well inside the high-density core of the halo gas profile and the shell will decelerate according to the Weaver et al. (1977) solution. However, for high injection density, the free expansion phase will continue for a longer time.

To illustrate this point, we plot in Fig. 2 the velocities of the forward shocks from two of our simulation runs (*MG6, MG7*), with higher ($n_{\rm inj} = 1.2$ cm^{-3}) and lower injection density ($n_{\rm inj} = 0.05$ cm^{-3}) respectively. We show the case of *MG6* with a dashed line and that of *MG7* with a dotted line and compare both with the slope $v_{\rm sh} \propto t^{-2/5}$ (solid line) expected for a stellar wind-blown bubble expanding in a uniform-density ISM. The case of *MG6* with large injection density shows less deceleration compared with *MG7*. If we consider a power-law density profile given by $n \propto r^{-m}$, then in the self-similar phase one would expect $r_{\rm sh} \propto t^{3/(5-m)}$ and $v_{\rm sh} \propto t^{-(2-m)/(5-m)}$. The halo gas profile (Fig. 1) beyond the

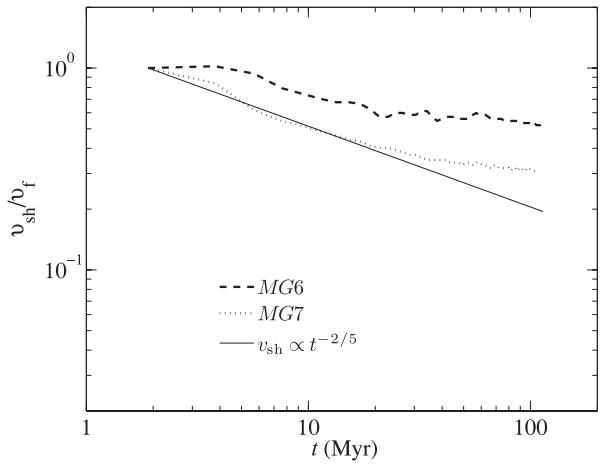

Figure 2. The velocity of the forward shock (v_{sh}) from our simulation runs *MG6* (dashed line) and *MG7* (dotted line) is compared with the self-similar solution for a stellar wind-blown bubble expanding in a uniform-density ISM (solid line). v_{sh} is shown in units of the velocity of free expansion, which is 10^3 km s^{-1} for *MG6* and *MG7*.

core region can be approximated as a power law decreasing with r, with index $m \sim 1$. One therefore expects $v_{sh} \propto t^{-0.25}$, implying only a mild decrease in velocity with time (or distance), which indeed is seen in Fig. 2 for the case of *MG6* (dashed line). For the case of *MG7* (dotted line), with low injection density, the final velocity is lower because it enters the self-similar phase at the core region of the halo density profile and therefore it exhibits a steeper decrease in velocity initially.

There is one regime in which our results should resemble the self-similar solution of the 'standard stellar wind bubble'. In an extreme situation, for very small values of r_f, the wind will decelerate quickly. We can quantify this regime in the following manner. The extent of the free expansion phase is small for low injection densities. Therefore, the evolution is governed mainly by the self-similar solution, for which the distance of the outermost shock is $r_{sh} = (Lt^3/\rho)^{1/5}$ and the corresponding velocity is $v_{sh} = 0.6(Lt^{-2}/\rho)^{1/5}$, where $\rho = nm_p$ is the density of the halo gas, the value of which is almost constant ($\sim 10^{-3}$ m_p cm^3) at small distances from the centre. Considering the inverse power-law dependence of velocity (v_{sh}) on time, it may happen that the wind travels a small distance and decelerates to negligible velocities. In such a case, there is no significant large-scale wind. Hence, for very low mechanical luminosities, when n_{inj} and v_{inj} are both small, we have a small-scale wind. Using the mechanical luminosity, $L = (1/2)4\pi n_{inj} m_p v_{inj}^3 r_b^2$, we can write the following general expression for r_{sh} in this case:

$$r_{sh} \approx 7\,\mathrm{kpc}\left(\frac{n_{inj}}{0.01\ \mathrm{cm}^{-3}}\right)^{1/2}\left(\frac{v_{inj}}{250\,\mathrm{km\,s}^{-1}}\right)^{3/2}\left(\frac{v_{sh}}{100\,\mathrm{km\,s}^{-1}}\right)^{-3/2}. \quad (6)$$

From the above equation, the larger the value of n_{inj} and v_{inj}, the larger will be the value of r_{sh}. If we assume that the wind decelerates to a small velocity, say $v_{sh} \approx 100$ km s^{-1}, before crossing $r_{sh} \approx 7$ kpc (i.e. the core of the gas density profile in the halo), then the corresponding values of n_{inj} and v_{inj} separate the cases of a small-scale wind bubble and the large-scale galactic wind. Note that the mechanical luminosity corresponding to the limiting case given by the above equation is $L \sim 10^{39}$ erg s^{-1}.

We also note that if n_{inj} is too large, such that the total energy lost per unit time due to radiative cooling ($\dot{E}_{cool}$) at the base is more than the energy injection rate at the base ($\dot{E}_{kin} \sim (1/2)m_p n_{inj} v_{inj}^3 4\pi r_b^2$), then it will lead to catastrophic cooling. To quantify this we can define the following ratio:

$$\frac{\dot{E}_{cool}}{\dot{E}_{kin}} \sim \frac{[(4\pi/3)r_b^3](n_{inj})^2\Lambda}{m_p n_{inj} v_{inj}^3 2\pi r_b^2} \sim \left(\frac{n_{inj}}{2\,\mathrm{cm}^{-3}}\right)\left(\frac{v_{inj}}{300\,\mathrm{km\,s}^{-1}}\right)^{-3}, \quad (7)$$

assuming $\Lambda \sim 10^{-22}$ erg cm^3 s^{-1}. We note that the above condition implies a critical mechanical luminosity of $L \sim 10^{42}(n_{inj}/2\,\mathrm{cm}^{-3})(v_{inj}/300\,\mathrm{km\,s}^{-1})^3$ erg s^{-1}, above which the cooling should dominate and in this case the outflow would be strictly momentum-driven.

4 THE SIMULATION RESULTS

Here we present the results from five of our runs. To start with, we show the case with no radiative cooling in Fig. 3, which clearly demonstrates the effect of the halo gas on the wind. One can see the formation of eddies at the periphery of the wind cone due to the relative motion between the wind gas and the halo gas and the onset of Kelvin–Helmholtz instability. This leads to turbulent mixing of gas in the halo. Note that the forward shock in this run reaches a distance of ∼20 kpc in the vertical direction by 47 Myr and shock-heats the ambient halo gas. At this time, there is a contact discontinuity at a vertical distance of ∼7 kpc, where one finds a slightly higher density. The region vertically below this contact discontinuity is occupied by shocked wind gas and heated by the reverse shock.

If a wind is launched with a radial injection in vacuum, it diverges geometrically as it reaches large distances. In other words, if the injection and the external forces are spherically symmetric then the wind will keep following the radial streamlines. In our case, although the wind is launched only with a z-component of velocity, the high pressure of the fluid ensures that the wind diverges as soon as it enters the box.

In this first case of ours, we can see in Fig. 3 that the wind cone does not diverge as much as it should have done if it were to expand freely in vacuum. It is halted at a distance of ∼7 kpc because of the resistance offered by the halo gas. The wind is not perfectly

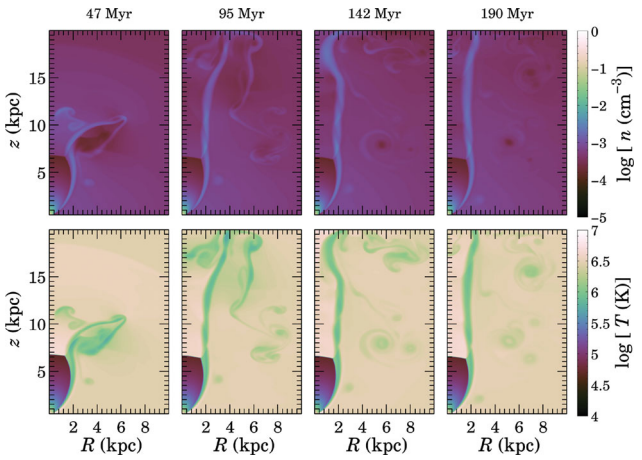

Figure 3. Time evolution of log density (upper panel) and log temperature (lower panel) in our first run, *MG1*, without radiative cooling. The wind injection velocity is 300 km s^{-1}.

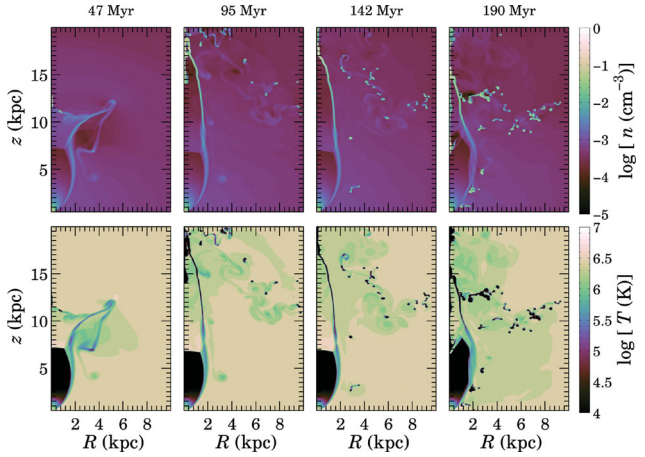

Figure 4. Time evolution of log density (upper panel) and log temperature (lower panel) in the run *MG2*. The wind injection velocity is 300 km s^{-1} and the injection density at the base is 0.1 cm^{-3}.

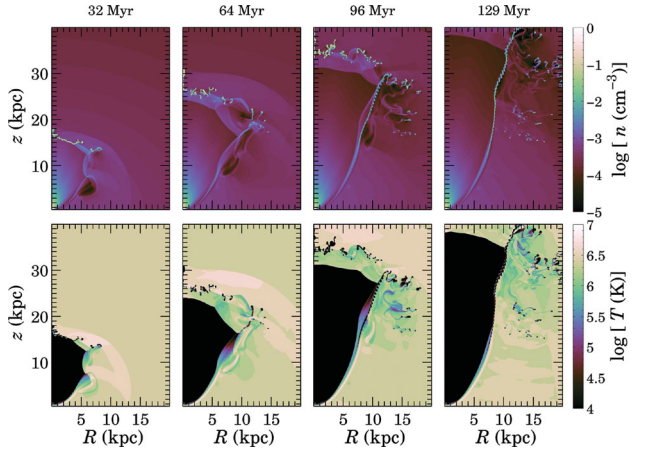

Figure 5. Time evolution of log density (upper panel) and log temperature (lower panel) in the run *MG3*. The wind injection velocity is 400 km s^{-1} and the injection density at the base is 1.0 cm^{-3}.

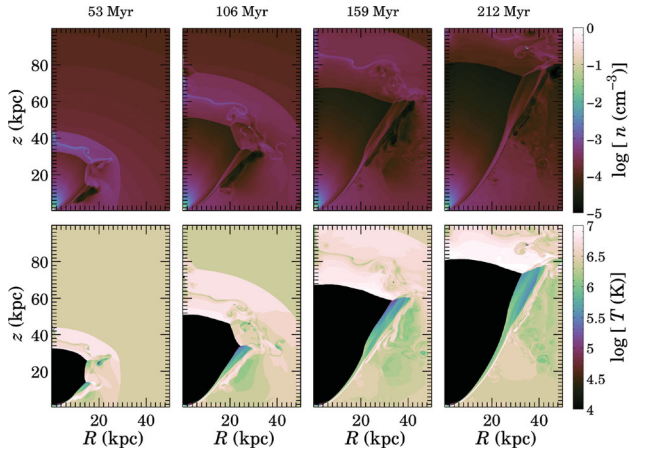

Figure 6. Time evolution of log density (upper panel) and log temperature (lower panel) in the run *MG4*. The wind injection velocity is 600 km s^{-1} and the injection density at the base is 2 cm^{-3}.

conical and the cross-sectional area becomes fixed roughly beyond ∼3 kpc. Previous studies have shown that the wind may or may not diverge with increasing distance, depending on how stratified the ambient medium is. It has been shown that if the ambient medium has an exponential or Gaussian density distribution then the wind also diverges, as it does in vacuum (Mac Low, McCray & Norman 1989). However, if the decrease in density is not steep, then one would expect a reduction in the cone width at large distances.

In Fig. 4, we show the density and temperature evolution for the case *MG2*, for which the injection density and velocity are the same as in the previous case; however, radiative cooling is switched on. An additional fact that is now evident is the formation of cold fragments in the high-density zones, which are the interaction zones between the halo and wind gas on the periphery of the wind cone. In this particular case ($n_{\rm inj}$ = 0.1 cm^{-3}, $v_{\rm inj}$ = 300 km s^{-1}), the cold clouds that form on the periphery of the eddies remain in the simulation box, but a few clouds that form on top of the wind cone escape the simulation box by the end of the run. These clouds do not form from the gas ejected from the disc alone, but mostly from the mixed gas in the interaction zone between the wind and halo gas. Therefore, in real galactic situations, if clouds form via this mechanism then they are likely to have a range of metallicities, similar to the case of high-velocity clouds in the Milky Way. This therefore represents a variation on the theme of a galactic fountain, but with the important difference that clouds form in the interaction between wind and halo gas.

Next, we increase the wind density and the size of the simulation box. In Fig. 5, we show the case of $n_{\rm inj}$ = 1 cm^{-3} and wind speed $v_{\rm inj}$ = 400 km s^{-1}. The enhanced wind momentum in this case is able to plough through the halo gas more effectively, as a result of which we see a diverging wind cone (in contrast to earlier cases). In this case, we have mostly forward-moving gas and even the clumps that form in the interaction zone ride with the flow in the simulation box. The clouds formed in this case represent the case of ram-pressure-driven clouds in superwinds.

The temperature plots in this run show temperatures less than 10^4 K in the entire wind cone. This has occurred due to strong cooling in this higher density case. This structure is an outcome of our assumption of a single injection site centred on the galaxy. In reality, the injection zones may be randomly distributed over the entire disc. In that case, the winds emerging from different injection zones will collide and there will be a more non-uniform density and temperature profile in the region above the disc plane (e.g. Melioli, de Gouveia Dal Pino & Geraissate 2013).

In Fig. 6, we increase the wind injection speed to 600 km s^{-1} and injection density to 2 cm^{-3} and we also increase the size of the simulation box, in order to study whether or not a wind with large injection speed can travel large distances and escape. In this case, the wind clears the simulation box in ∼200 Myr. The additional momentum pushes the compressed shell further into the halo, where the shell gas is diluted and does not fragment into clouds.

Finally, in Fig. 7 we decrease the wind density and keep an injection velocity of 500 km s^{-1} in a box height of 100 kpc. In this case, radiative cooling is not so effective as in the previous case because of lower density. Also, the wind cannot escape because at some height the wind density falls below that of the halo gas. As a combined effect of these two aspects, we have regions of low-density warm gas (10^5–10^6 K) present in the halo, as shown in the density and temperature snapshots. The column density of this warm gas is $\geq 10^{18}$ cm^{-2}, for a density of $\sim 10^{-4}$ cm^{-2} and a length-scale of ∼10 kpc. Hence these regions are likely candidates for O VI absorption systems, observed repeatedly in the past as a circumgalactic medium in the haloes of galaxies (Sembach et al. 2003; Savage et al. 2003; Tumlinson et al. 2011).

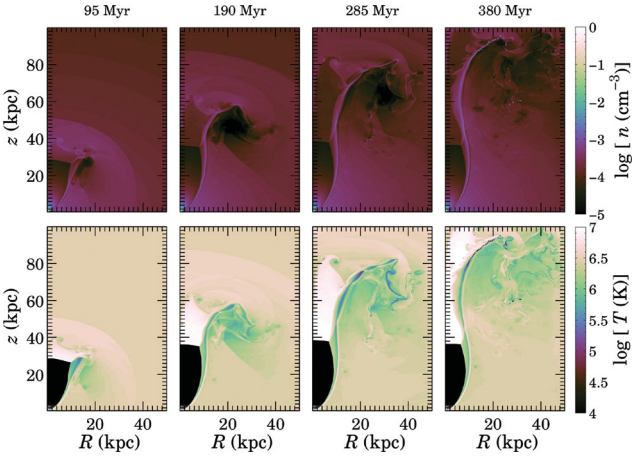

Figure 7. Time evolution of log density (upper panel) and log temperature (lower panel) in the run *MG5*. The wind injection velocity is 500 km s^{-1} and the injection density at the base is 0.5 cm^{-3}.

Note that a warm–hot phase (10^5–10^6 K) is also present in other cases. For example, if we look at the temperature profiles of clouds for *MG2* and *MG3* in the lower panels of Figs 4 and 5, they have a wake of warm gas behind them, which appears greenish and roughly corresponds to a temperature of $10^{5–6}$ K. The presence of a warm–hot medium in the wakes of high-velocity clouds was also suggested recently by Marasco, Marinacci & Fraternali (2013). Furthermore, observations suggest that HVCs contain different species from ionized to neutral (Lehner et al. 2012; Thom et al. 2012). We suggest that different species can be explained by considering the variation of temperature around the cloud centre (e.g. in the wake of the cloud). Furthermore, the temperature snapshots of *MG1* (the simulation run without cooling) show regions with gas at $\sim 10^{5.5}$ K, which implies that if the cooling is suppressed (possibly in systems with low metallicities), one can also generate O VI absorption systems simply by adiabatic cooling of galactic wind gas confined inside the halo.

We plot the gas velocities as a function of the vertical distance for four snapshots in cases *MG2* (top left panel), *MG3* (top right), *MG4* (bottom left) and *MG5* (bottom right) in Fig. 8. The wind speed initially increases to a value almost double the injection speed, as expected in a steady (transonic) wind case (Sharma & Nath 2013) and explained in Section 2.2. The wind speed then drops to a low value at a certain distance because of the interaction with halo gas. This signifies the boundary between the steady wind and shocked wind that arises due to a reverse shock. Then, depending on the efficiency of cooling, there is formation of a thin shell, which becomes momentum-driven, and a consequent rise in the velocity is seen. In contrast, for the case of low cooling efficiency (bottom right panel for run *MG5*), the shocked region is thick and the existence of thin shells is not apparent in the velocity plot.

Another important point to note in the velocity plots is the effect of the halo gas in decelerating the wind front. Compare the bottom left and bottom right panels, for high injection speeds. With a lower injection density in the bottom right panel, we find that the wind is stuck at ∼40 kpc even when the injection speed is large enough to overcome the gravitational potential barrier. This is an example in which the wind is contained within the halo due to the resistance offered by the halo gas. This aspect is also clear from our discussion in Section 3, where in Fig. 2 we have plotted the velocities of the forward shocks for *MG6* and *MG7* using dashed and dotted lines. Although these two runs have same injection speed, still for *MG7*

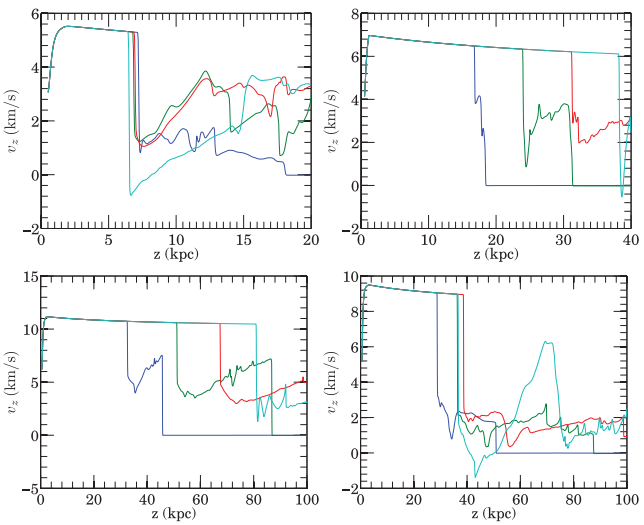

Figure 8. Velocity along the z-axis in the computational box at four different times for our runs *MG2* (top left), *MG3* (top right), *MG4* (bottom left) and *MG5* (bottom right). For each run, four curves are shown with colours blue, green, red and cyan in increasing order of simulation time. The simulation times are the same as used in the density and temperature plots. A colour version of this figure is available in the online version of the article.

the velocity of the forward shock becomes almost half of that in *MG6*.

We point out that the wind gas cools but does not fragment, while fragmentation occurs only in the dense shell. The reason is that thermal instability grows quickly in the compressed high-density region, while the wind gas diverges on account of its speed and becomes dilute after entering the simulation box and the low density does not favour thermal instability.

4.1 Cloud properties

Here we determine the properties of the clouds formed in our simulations. In this regard, we estimate the size and mean density of the clouds. Numerically, this is achieved in a few steps, in which we first consider a particular snapshot of the simulation and find all the local maxima in density. Then we define circles of radius R_c centred at the position of the local maxima. We start with a minimum value of R_c that is greater than the size of the smallest computational cell in the simulation and calculate the average density in the circular region. We then keep increasing the value of R_c and determine the average density ($\langle n_c \rangle$) as a function of R_c.

The result is shown in the left and right panels of Fig. 9, corresponding to runs *MG2* and *MG3* at $t = 180$ Myr, respectively.

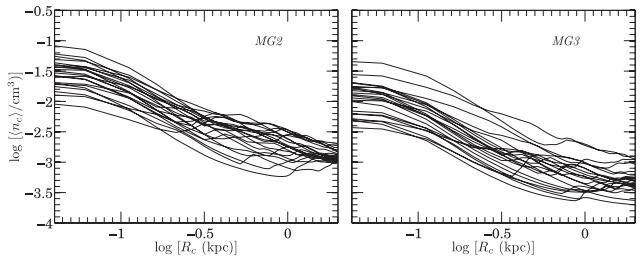

Figure 9. The mean density ($\langle \rho_c \rangle$) in a circle centred on the cloud and having radius R_c is plotted versus R_c. Results for runs *MG2* and *MG3* corresponding to time $t = 180$ Myr are shown in the left and right panels, respectively.

Each line in the plot corresponds to a single cloud. We can see that, for small values of R_c, the densities are high and they decrease slowly with R_c, as we sample the inner high-density region of the cloud and move slowly outward. Afterwards, there is a steep fall in density with R_c as we move out of the cloud region. In the end, the density decreases slowly once again when R_c has become large and the mean density is determined by the gas surrounding the cloud. The size of the cloud is roughly in the range 100–500 pc, as inferred from the steeper part of the curves when the density decreases rapidly, which implies a transition from a high-density cloud to a low-density ambient medium. The estimated size of the clouds ($\gtrsim$100) is greater than the smallest cell size in our simulation, which is 40 pc. Also, this estimate for cloud size is consistent with the sizes expected from thermal instability, $t_{\rm cool} \times c_s$, since $t_{\rm cool} \sim 3$–10 Myr and $c_s \sim 10$–30 km s^{-1}.

The average density of the clouds ($\langle n_c \rangle$) is in the range 10^{-2}–10^{-1} cm^{-3}. The mass of the cloud can be calculated using $M_c = (4\pi/3)\langle n_c \rangle m_p R_c^3$, which yields $M_c = 10^3$–10^5 M$_\odot$. Considering the fact that roughly $\sim 10^2$ clouds are present in the simulation box, we find that the total mass in clouds is $M_{\rm total,clouds} \sim 10^5$–$10^7$ M$_\odot$. We note that observations also find a similar amount of mass contained in HVCs (Wakker et al. 2007), although in the simulations the total mass in HVCs is model-dependent. We mention here that a few of the curves in Fig. 9 show an abrupt upturn for large R_c, which is due to the presence of a neighbouring cloud.

Next, we explore the velocity of the high-velocity clumps formed in our simulations. We determine the velocity of regions with density $n > 0.02$ cm^{-3} in the galactic standard of rest (GSR) frame. We plot the histogram of the velocities thus obtained in Fig. 10. The three plots in the left column of the figure correspond to *MG2* and the three plots in the right column represent *MG3*. We have shown the velocity distribution at three different epochs, $t = 95, 190$ and 304 Myr, from top to bottom respectively.

For the case of *MG2* (left column), we obtain a normal distribution for the velocities. It is interesting to note that observations of HVCs in the Galaxy also indicate a normal distribution of velocities in the GSR frame, with a mean velocity of ≈ -50 km s^{-1} (Blitz et al. 1999). The span of velocities of HVCs is generally $\gtrsim$100 km s^{-1} (Putman et al. 2002), which is larger than the range of cloud velocities in this simulation. Therefore, the clouds formed in the present simulations are better compared with intermediate-velocity clouds (IVCs). We can speculate that infalling clouds in the Milky Way may have been created within the last $\sim$100 Myr, since the upper left panel does show a significant contribution to negative velocities. It is also possible that the halo gas distribution in the Milky Way differs from the simple profile assumed here, which may lead to differences in the dynamics of the clouds. A detailed comparison of clouds formed in this formalism with the properties of IVCs/HVCs deserves a separate study. In the case of our run *MG3* (right column), we find that a significant number of clouds have a positive velocity with respect to the galactic centre. The distribution appears to be bimodal, with a normal component centred at a mean velocity of roughly zero and another component having positive velocity, indicating outflow. This is because of the fact that the mechanical luminosity of the injected wind in the case of *MG3* is high, resulting in a greater number of outflowing clouds.

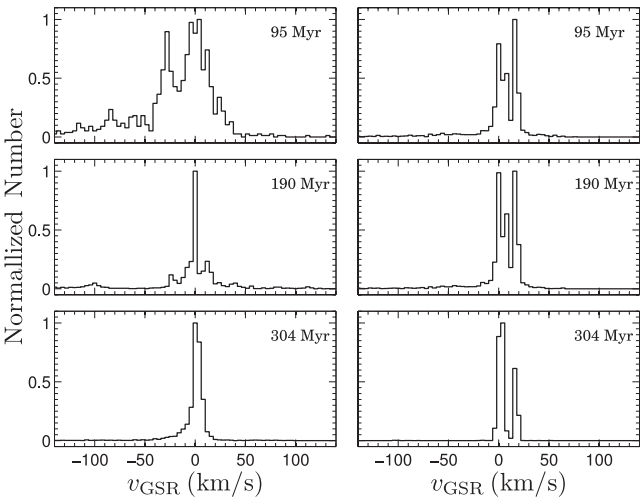

Figure 10. Normalized number of high-density zones (clouds) as a function of the velocity in the galactic standard of rest frame. The left panel corresponds to our run *MG2* at various times of evolution and the right panel corresponds to *MG3*.

We conclude that, with a suitable combination of $n_{\rm inj}$ and $v_{\rm inj}$, which in turn depend on the SFR, wind-loading factor and efficiency of energy injection from SNe, one can explain the properties of infalling clouds in quiescent galaxies such as the Milky Way and outflowing cold clouds in galaxies with high SFR such as ULIRGs.

5 DISCUSSION

We summarize our results by representing the outcome of different simulation runs in the parameter space $n_{\rm inj}$–$v_{\rm inj}$ in Fig. 11. For this purpose, we use the results of all our runs mentioned in Table 1, besides the ones discussed in the previous section. Based on our discussions so far, we can first exclude two regions that do not show significant amounts of multiphase extraplanar gas. These comprise the following.

(i) *Small-scale wind bubble*. As discussed at the beginning of our analytical estimates (Section 3), if the shell decelerates to negligible speeds within a distance $\sim$10 kpc then the wind is confined to small scales and we refer to the case as a small-scale wind bubble. At later times, the wind material in this case collapses on itself. We mark this case with an open circle in Fig. 11. We also note that, for cases such as these, the efficiency of energy injection in the wind and the wind mechanical luminosity would also be unphysically small ($\epsilon \approx 10^{-2}, L_{\rm mech} \lesssim 10^{39}$ erg s^{-1}). The limiting combination of $n_{\rm inj}$ and $v_{\rm inj}$ that leads to such cases can be obtained from equation (6) by requiring $r_{\rm sh} \leq 7$ kpc; one finds a scaling $v_{\rm inj} \propto n_{\rm inj}^{-1/3}$, which divides this small-scale wind from the galactic wind. We show this limiting combination as a dashed line in the bottom left corner of Fig. 11.

(ii) *Catastrophic cooling*. If the injection density is very large, then energy loss by cooling can be catastrophic and the wind material enters the simulation box and cools quickly before it can diverge into a cone. Two of our simulation runs (*MG14* and *MG15*) show this characteristic and are marked by open squares in Fig. 11. The corresponding criteria for the onset of catastrophic cooling can be inferred from equation (7) by setting $\dot{E}_{\rm cool} < \dot{E}_{\rm kin}$. The boundary line for this case has a scaling $v_{\rm inj} \propto n_{\rm inj}^{1/3}$ and is shown in Fig. 11 by a dash–dotted line.

Apart from the combination of $n_{\rm inj}$ and $v_{\rm inj}$ for the above two regions, we find significant fragmentation in the interaction zones in other cases. In our runs *MG2* and *MG3*, the interaction zone fragments rapidly into cold clouds of $T \sim 10^4$ K. In *MG2*, as the wind gas ploughs through the halo gas, eddies are formed in the side walls due to the relative motion. These eddies break out of the bulk flow and form cool clouds. As discussed earlier, we

have found the total mass enclosed in these clouds to be $\sim 10^5$–10^7 $M_\odot$ and they extend out to $\sim$10 kpc from the Galactic Centre. These clouds resemble IVCs/HVCs and we mark these cases with downward-pointing triangles in Fig. 11.

If the injection speed and density are high, as in *MG3*, then the wind cone diverges up to a large distance. The clouds formed in these cases (marked with diamonds in Fig. 11) are entrained in the bulk flow. Therefore a large number of clouds have a positive velocity outward from the Galactic Centre, as indicated by the velocity histogram in the right panel of Fig. 10. We note that these cases resemble the scenario of cold clouds embedded in steady winds (Sharma & Nath 2012; Murray et al. 2011).

In our run *MG5*, the interaction between the wind and the halo gas leads to significant regions of warm–hot (10^5–10^6 K) gas and in this case cooling is not effective enough to produce cold clumps. The column density of the warm–hot gas in this case is sufficiently large to explain the observed O VI absorption, as discussed earlier. We mark cases similar to *MG5* in Fig. 11 with filled circles. We note here that the 10^5–10^6 K gas is also visible in the wakes behind the moving clouds in our runs *MG2* and *MG3*, which can also give rise to O VI absorption (see also Marasco et al. 2013).

Finally, if the wind density and speed are further increased, then the wind crosses 100 kpc (our simulation box) and possibly escapes the virial radius. The runs that show these features are marked by upward-pointing triangles in the top right corner of Fig. 11. The shell in this case fragments as well, if the density is sufficiently high, and clumps can be driven into the IGM. These cases are responsible for the metal enrichment of the IGM (Nath & Trentham 1997; Madau, Ferrara & Rees 2001; Samui, Subramanian & Srianand 2008).

The mass-loading rate in the wind can be written as $\dot{M} \sim (4\pi r_b^2) m_p n_{inj} v_{inj}^3$. The mass-loading rate is related to the SFR($\dot{M} = \eta$ SFR) and values of this quantity for our runs are provided in Table 1. Here in Fig. 11 we have plotted this quantity using a colour code for increasing $\dot{M}$ from dark green to bright yellow. If we consider a constant η, then the dark green regions correspond to low SFR and the bright yellow regions to high SFR. We can see that the simulation runs producing CGM fall mostly in the low SFR region. The escaping winds and wind-embedded clouds occupy the high SFR zones and the infalling cold clouds occupy the intermediate-SFR regions. The Milky Way, with SFR $\sim 3\ M_\odot\ yr^{-1}$ and considering a low $v_{wind} = 2v_{inj}$, should occupy the lower central region of Fig. 11. The result that this region is dominated by infalling clouds in our simulations agrees with the observations of IVCs/HVCs in our Galaxy. We note that from Table 1, for the Milky Way SFR and for our run *MG2*, we obtain $\eta \sim 1$, which implies $\dot{M} \sim$ SFR. Also, the efficiency of energy injection, $\epsilon \sim 0.2$, is small and consistent for a quiescent galaxy such as the Milky Way. We further note that, from Fig. 11, one can infer the value of mass loading factor (η) for a galaxy with a given SFR and observed morphology of extraplanar gas. Similarly, one can determine ϵ by using the relation $\epsilon = 0.8\eta(v_{inj}/500\ km\ s^{-1})^2$. Therefore this figure can be used in conjunction with equations (3) and (4) as a diagnostic to find physical values of wind parameters such as η and ϵ, by matching with observations.

We have also shown three contours (solid lines) of constant $\dot{M}$, corresponding to $\dot{M} = 10^0, 10^1, 10^2\ M_\odot\ yr^{-1}$ from left to right respectively. These contours help us to draw important conclusions about the possible values of η and SFR. For example, cold clouds and CGM are likely to appear when the wind mass-loading rate is $\sim$1–10 $M_\odot\ yr^{-1}$ and outflowing clouds and escaping winds are possible when the mass-loading rate is $\sim$10–100 $M_\odot\ yr^{-1}$. This also

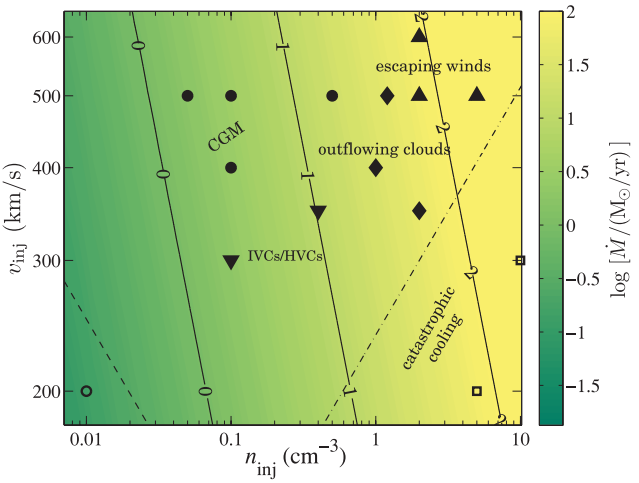

Figure 11. Simulation runs in the parameter space of n_{inj} and v_{inj}. The dashed and dash–dotted lines represent the boundaries of regions for small-scale wind bubbles (bottom left corner) and catastrophic cooling (bottom right corner) respectively. The logarithm of wind mass-loading rate ($\dot{M} = \eta \times$ SFR) is shown by colour coding, with bright yellow regions representing large values of $\dot{M}$. Three parallel solid lines are the contours corresponding to $\log(\dot{M}/M_\odot\ yr^{-1}) = 0, 1, 2$ from left to right respectively. A colour version of this figure is available in the online version of the article.

agrees with observations, where cold clumpy outflows are observed in galaxies with high star-formation rates (e.g. Martin 2005).

There is yet another interpretation to this figure. If we consider that the SFR is fixed and the mass loading (η) varies in the plot box, then the left part of the figure represents weak winds with small mass loading and the right part a highly loaded wind. The central part of Fig. 11 is the place where the wind has an optimum value of mass loading, so as to have physically plausible winds that can explain the cold clumpy extraplanar media in galaxies.

If we assume that the initial stage of galactic evolution is marked by high SFR, then we expect those galaxies to occupy the top right corner of Fig. 11, the region of escaping winds. As the galaxy loses gas via these escaping winds, the SFR decreases and one enters regions either to the left or bottom left of Fig. 11, depending on the rate of decrement of SFR. This will determine whether or not these galaxies should have a significant amount of CGM or infalling clouds (which may sustain the SFR). Therefore the interaction between the wind and the halo gas is a crucial factor in galactic evolution.

Thermal instability is suppressed in a freely expanding galactic wind (Ferrara & Einaudi 1992). Recent simulations show that clouds also cannot condense spontaneously from the hot gas in the halo (Joung, Bryan & Putman 2012; Hobbs et al. 2013). However, here we have found that clouds can condense in the compressed region formed due to galactic outflow punching through the halo gas. Therefore, this work can be considered a hybrid scenario of cloud formation from galactic outflows (fountains) and/or cloud condensation from a stationary or infalling halo gas.

We would like to point out the following limitations of our simulations. We have assumed a uniform metallicity throughout the simulation box, although, at large scales inside the halo, the metallicity can vary. This may have led to an overestimation of cooling in these calculations. However, we also note that these simulations are in two dimensions, for which the effect of cooling is underestimated. Gas metallicity at large distances from the plane is expected

to be lower than in the disc, although it is not clear by how much. For such conditions, all the features of an expanding wind bubble would be similar except that the transition of the shock front to the radiative phase will take longer. We wish to address these issues in a future article.

6 SUMMARY

We have simulated the interaction of a galactic wind with hot halo gas. We have found that the wind drives a shell of compressed gas, which fragments due to instabilities and leads to the formation of infalling and/or outflowing clouds as well as O VI regions, depending on the amount of cooling. We have categorized the formation of various multiphase media in the parameter space of injection velocity and density, which are the input parameters for our simulations. We have found that clouds formed in our simulations have a total mass of 10^5–10^7 $M_\odot$ and have a distribution of velocity. For higher density and velocity of injection, corresponding to vigorously star-forming galaxies, a significant number of clouds are outflowing. Furthermore, circumgalactic material with a temperature in range 10^5–10^6 K is also seen in our simulations, with a column density appropriate to give rise to the observed O VI absorption. These results lead to the conclusion that infalling clouds, cold clumpy outflows and the circumgalactic medium can form due to the interaction of galactic wind with the halo gas. The injection density and velocity are linked with the SFR, mass-loading factor of outflows and efficiency of energy injection by SNe. Therefore, the results deduced in these simulations may serve as a diagnostic to constrain the feedback efficiency of outflows.

ACKNOWLEDGEMENTS

The authors acknowledge support from an Indo-Russian project (RFBR grant 12-02-92704-IND, DST-India grant INT-RFBR-P121). For the plots in this work, we have used the 'Cubehelix' colour scheme described in Green (2011). We thank P. Sharma and E. Vasiliev for helpful discussions. We thank an anonymous referee for constructive comments on the manuscript.

REFERENCES

Anderson M. E., Bregman J. N., 2010, ApJ, 714, 320
Binney J., 1977, ApJ, 215, 483
Binney J., Nipoti C., Fraternali F., 2009, MNRAS, 397, 1804
Birnboim Y., Dekel A., 2003, MNRAS, 345, 349
Blitz L., Spergel D. N., Teuben P. J., Hartmann D., Burton W. B., 1999, ApJ, 514, 818
Bregman J. N., 1980, ApJ, 236, 577
Burke J. A., 1968, MNRAS, 140, 241
Chabrier G., 2003, PASP, 115, 763
Chattopadhyay I., Sharma M., Nath B. B., Ryu D., 2012, MNRAS, 423, 2153
Chevalier R. A., Clegg A. W., 1985, Nature, 317, 44
Dalla Vecchia C., Schaye J., 2008, MNRAS, 387, 1431
Fang T., Bullock J., Boylan-Kolchin M., 2013, ApJ, 762, 20
Ferrara A., Einaudi G., 1992, ApJ, 395, 475
Fukugita M., Hogan C. J., Peebles P. J. E., 1998, ApJ, 503, 518
Green D. A., 2011, Bull. Astron. Soc. India, 39, 289
Hagihara T., Yao Y., Yamasaki N. Y., Mitsuda K., Wang Q. D., Takei Y., Yoshino T., McCammon D., 2010, PASJ, 62, 723
Hobbs A., Read J., Power C., Cole D., 2013, MNRAS, 434, 1849
Hopkins P. F., Quataert E., Murray N., 2012, MNRAS, 421, 3522
Johnson H. E., Axford W. I., 1971, ApJ, 165, 381
Joung M. R., Bryan G. L., Putman M. E., 2012, ApJ, 745, 148
Kauffmann G., Heckman T. M., De Lucia G., Brinchmann J., Charlot S., Tremonti C., White S. D. M., Brinkmann J., 2006, MNRAS, 367, 1394
Kompaneets A. S., 1960, Sov. Phys. Doklady, 5, 46
Lehner N., Howk J. C., Thom C., Fox A. J., Tumlinson J., Tripp T. M., Meiring J. D., 2012, MNRAS, 424, 2896
Mac Low M.-M., Ferrara A., 1999, ApJ, 513, 142
Mac Low M.-M., McCray R., Norman M. L., 1989, ApJ, 337, 141
Madau P., Ferrara A., Rees M. J., 2001, ApJ, 555, 92
Majumdar S., Nath B. B., Chiba M., 2001, MNRAS, 324, 537
Maller A. H., Bullock J. S., 2004, MNRAS, 355, 694
Marasco A., Marinacci F., Fraternali F., 2013, MNRAS, 433, 1634
Marcolini A., Strickland D. K., D'Ercole A., Heckman T. M., Hoopes C. G., 2005, MNRAS, 362, 626
Marinacci F., Binney J., Fraternali F., Nipoti C., Ciotti L., Londrillo P., 2010, MNRAS, 404, 1464
Marinacci F., Fraternali F., Nipoti C., Binney J., Ciotti L., Londrillo P., 2011, MNRAS, 415, 1534
Martin C. L., 2005, ApJ, 621, 227
Melioli C., de Gouveia Dal Pino E. M., 2004, A&A, 424, 817
Melioli C., de Gouveia Dal Pino E. M., Geraissate F. G., 2013, MNRAS, 430, 3235
Mignone A., Bodo G., Massaglia S., Matsakos T., Tesileanu O., Zanni C., Ferrari A., 2007, ApJS, 170, 228
Murray N., Quataert E., Thompson T. A., 2005, ApJ, 618, 569
Murray N., Ménard B., Thompson T. A., 2011, ApJ, 735, 66
Nath B. B., Silk J., 2009, MNRAS, 396, L90
Nath B. B., Trentham N., 1997, MNRAS, 291, 505
Navarro J. F., Frenk C. S., White S. D. M., 1997, ApJ, 490, 493
Pickelner S. B., Shklovsky I. S., 1958, Rev. Mod. Phys., 30, 935
Putman M. E. et al., 2002, AJ, 123, 873
Putman M. E., Peek J. E. G., Joung M. R., 2012, ARA&A, 50, 491
Rasmussen J., Sommer-Larsen J., Pedersen K., Toft S., Benson A., Bower R. G., Grove L. F., 2009, ApJ, 697, 79
Rossa J., Dettmar R.-J., Walterbos R. A. M., Norman C. A., 2004, AJ, 128, 674
Samui S., Subramanian K., Srianand R., 2008, MNRAS, 385, 783
Savage B. D. et al., 2003, ApJS, 146, 125
Sembach K. R. et al., 2003, ApJS, 146, 165
Shapiro P. R., Field G. B., 1976, ApJ, 205, 762
Sharma M., Nath B. B., 2012, ApJ, 750, 55
Sharma M., Nath B. B., 2013, ApJ, 763, 17
Sharma M., Nath B. B., Shchekinov Y., 2011, ApJ, 736, L27
Silk J., 1977, ApJ, 211, 638
Spitzer L., Jr, 1956, ApJ, 124, 20
Strickland D. K., Heckman T. M., Colbert E. J. M., Hoopes C. G., Weaver K. A., 2004, ApJS, 151, 193
Suchkov A. A., Balsara D. S., Heckman T. M., Leitherer C., 1994, ApJ, 430, 511
Suchkov A. A., Berman V. G., Heckman T. M., Balsara D. S., 1996, ApJ, 463, 528
Sutherland R. S., Dopita M. A., 1993, ApJS, 88, 253
Swaters R. A., Sancisi R., van der Hulst J. M., 1997, ApJ, 491, 140
Teşileanu O., Mignone A., Massaglia S., 2008, A&A, 488, 429
Thom C. et al., 2012, ApJ, 758, L41
Tomisaka K., Bregman J. N., 1993, PASJ, 45, 513
Tumlinson J. et al., 2011, Science, 334, 948
van Woerden H., Wakker B. P., 2004, in van Woerden H., Wakker B. P., Schwarz U. J., de Boer K. S., eds, Astrophysics and Space Science Library, Vol. 312, High Velocity Clouds. Kluwer, Dordrecht, p. 195
Veilleux S., Cecil G., Bland-Hawthorn J., 2005, ARA&A, 43, 769
Veilleux S., Rupke D. S. N., Swaters R., 2009, ApJ, 700, L149
Voigtländer P., Kamphuis P., Marcelin M., Bomans D. J., Dettmar R.-J., 2013, A&A, 554, A133
Wakker B. P., Savage B. D., Sembach K. R., Richter P., Fox A. J., 2005, in Braun R., ed., ASP Conf. Ser. Vol. 331, Extra-Planar Gas. Astron. Soc. Pac., San Francisco, p. 11
Wakker B. P. et al., 2007, ApJ, 670, L113
Wang B., 1995, ApJ, 444, 590

Wang Q. D., 2001, in Funes J. G., Corsini E. M., eds, ASP Conf. Ser. Vol. 230, Galaxy Disks and Disk Galaxies. Astron. Soc. Pac., San Francisco, p. 393
Wang Q. D., 2007, in Emsellem E., Wozniak H., Massacrier G., Gonzalez J.-F., Devriendt J., Champavert N., eds, EAS Publ. Ser., Vol. 24, Chemodynamics: From the First Stars to Local Galaxies. Cambridge Univ. Press, Cambridge, p. 59
Weaver R., McCray R., Castor J., Shapiro P., Moore R., 1977, ApJ, 218, 377
White S. D. M., Frenk C. S., 1991, ApJ, 379, 52
White S. D. M., Rees M. J., 1978, MNRAS, 183, 341

This paper has been typeset from a TEX/LATEX file prepared by the author.